Supplementary Information

Zebrafish chemical screening reveals an inhibitor of Dusp6 that expands cardiac cell lineages

Gabriela Molina[1,7,8], Andreas Vogt[2,6,8], Ahmet Bakan[3,8], Weixiang Dai[4], Pierre Queiroz de Oliveira[2], Wade Znosko[1], Thomas E. Smithgall[1,6], Ivet Bahar[3,6], John S. Lazo[2,6], Billy W. Day[4,5] & Michael Tsang[1,9]

[1]Departments of Microbiology and Molecular Genetics, [2]Pharmacology and Chemical Biology, [3]Computational Biology, [4]Pharmaceutical Sciences and [5]Chemistry, and [6]Pittsburgh Molecular Libraries Screening Center, University of Pittsburgh, 3501 Fifth Ave, BST3-5062. Pittsburgh, PA 15213, USA. [7]Current address: SRI, Center for Advanced Drug Research, Harrisonburg, VA, USA. [8]These authors contributed equally to this work. [9]Correspondence should be addressed to M.T. (tsang@pitt.edu)

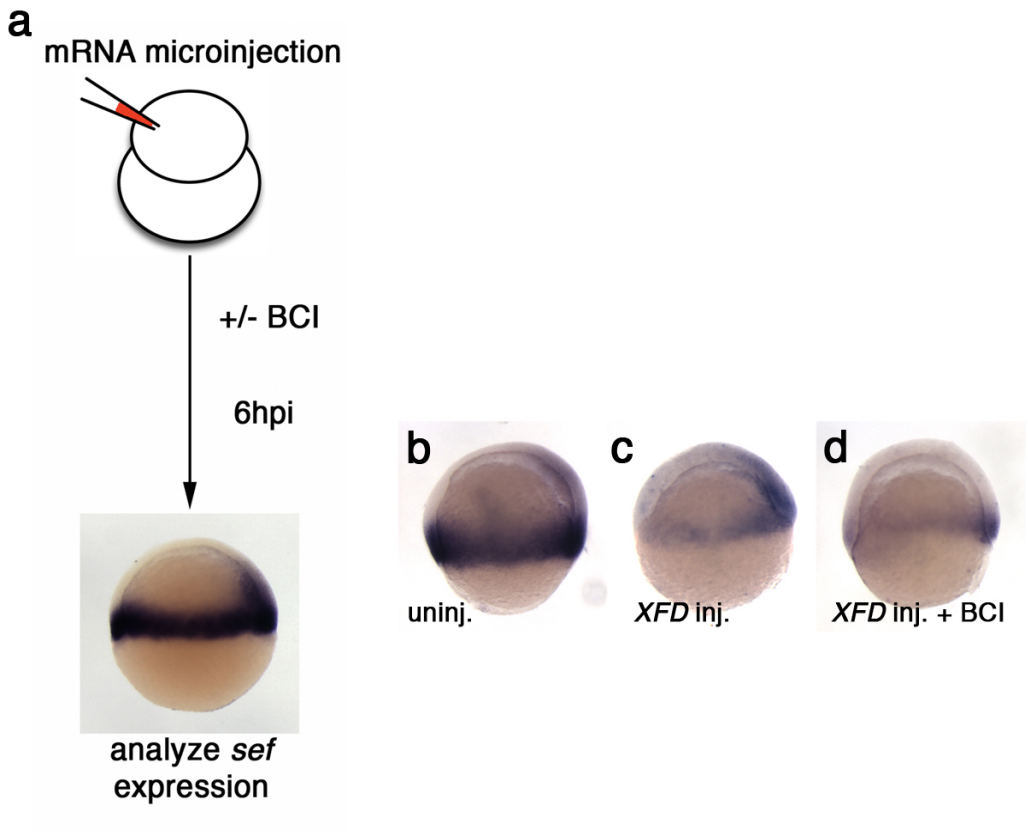

Supplementary Figure 1

Ectopic expression assay to identify BCI target

(**a**) Experimental plan depicting microinjection of mRNA into 1-cell stage embryos and analysis of FGF activity as measured by *sef* expression. (**b-d**) Lateral view of Shield stage embryos stained showing *sef* expression as a marker for FGF activity. (**b**) uninjected control. (**c**) Embryo injected with *XFD* mRNA shows a marked reduction of *sef* expression. (**d**) embryo injected with *XFD*, followed by incubation with 5 μM BCI did not restore *sef* expression.

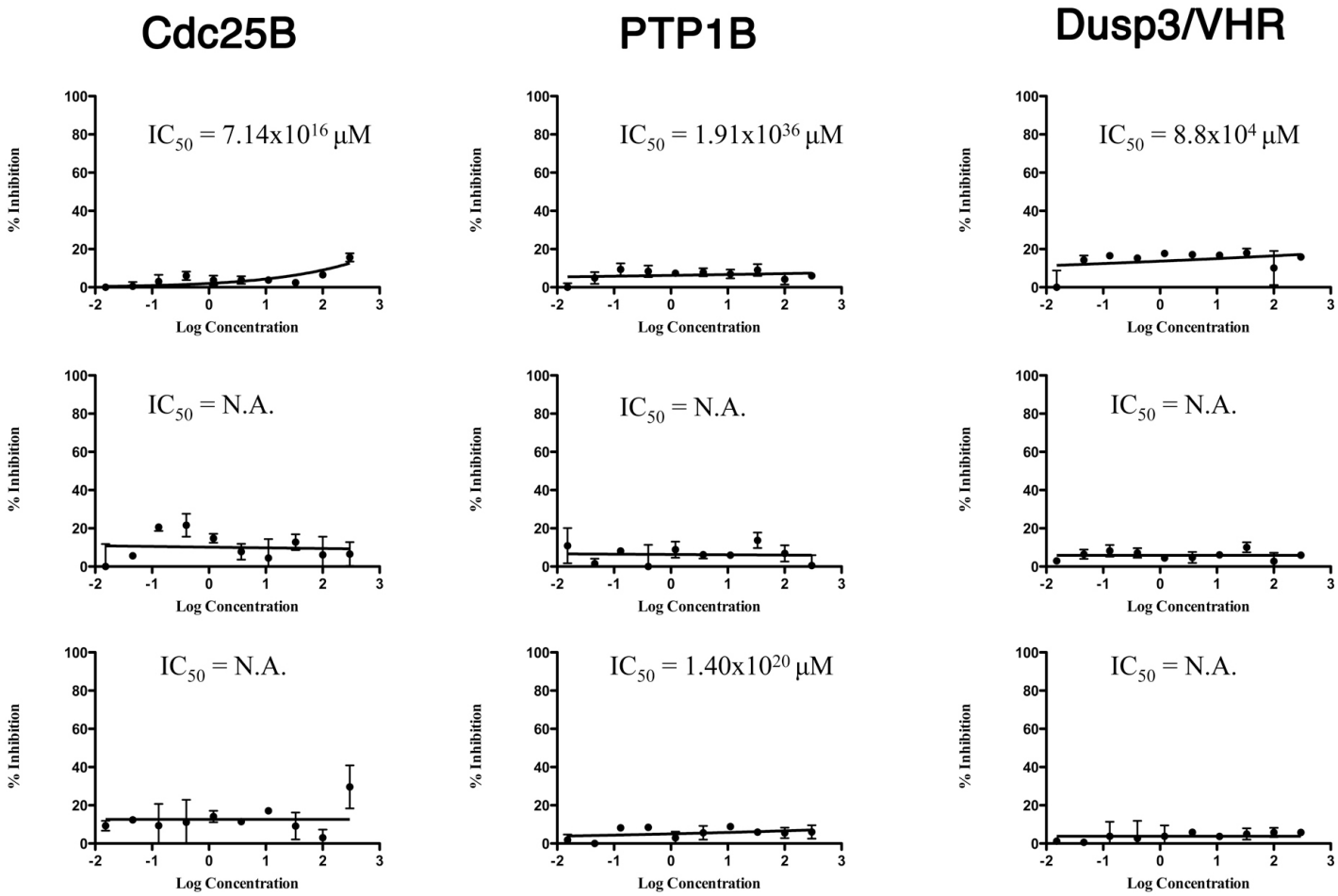

Supplementary Figure 2

BCI does not inhibit Cdc25B, PTP1B or Dusp3/VHR.

Recombinant enzymes were incubated with OMFP in the presence of increasing concentrations of BCI (15.2 nM – 300 µM). BCI exhibited no activity in suppressing phophatase activity by these enzymes. in vitro assays was tested in triplicates (individual graph represents a single experiment) for each phosphatase. 100 µM Sodium Orthovanadate completely inhibited all three phosphatases and represented 100% inhibition.

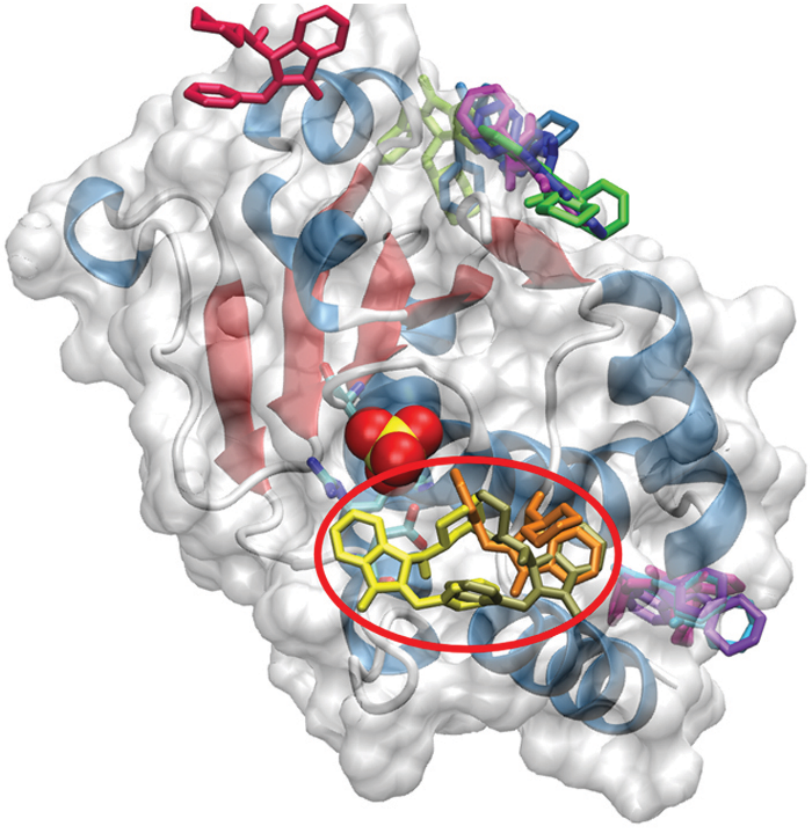

Supplementary Figure 3

Unbiased docking solutions for high-activity state model of Dusp6.

Nature Chemical Biology: doi:10.1038/nchembio.190

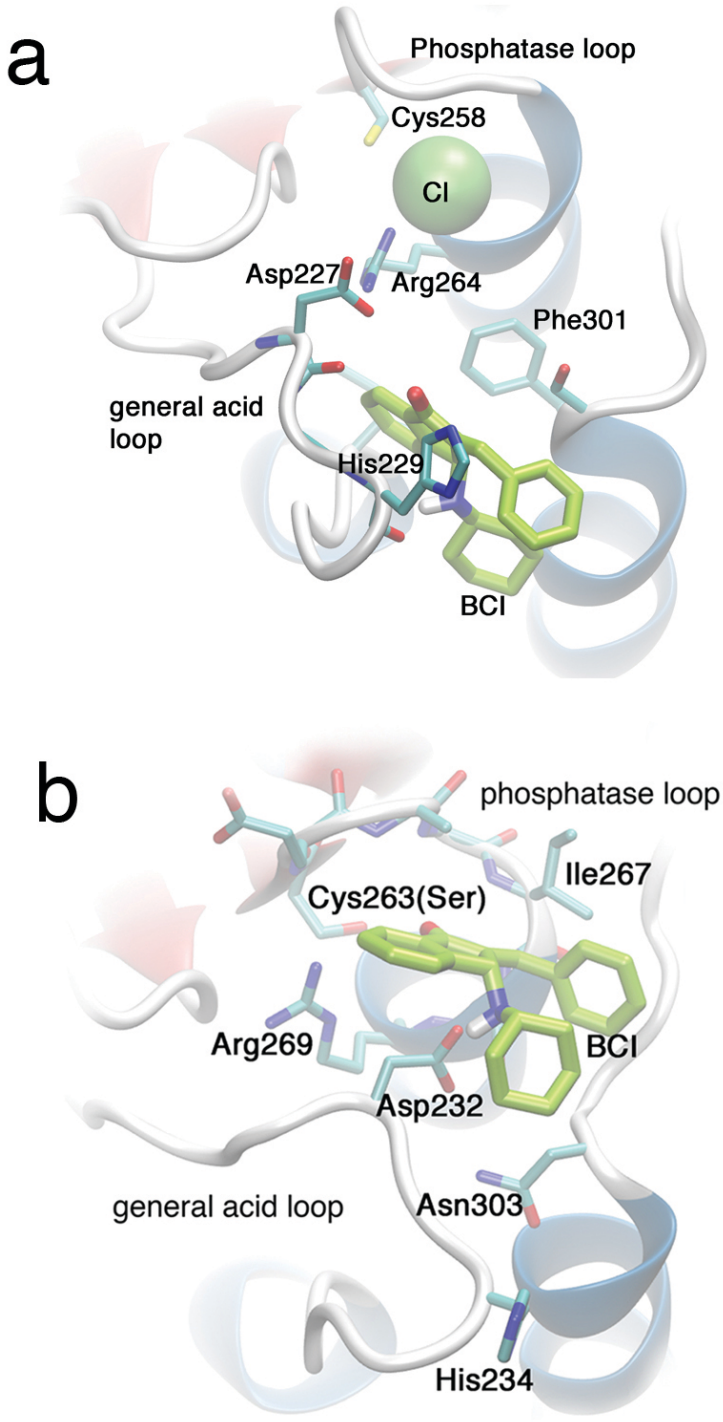

Supplementary Figure 4

Docking solutions for Dusp1 and Dusp5. (**a**) BCI fits within a similar Dusp6 crevice in low-activity state of Dusp1 and exhibits comparable interactions. **(b)** Docking solution for Dusp5 shows weak interaction within the catalytic pocket.

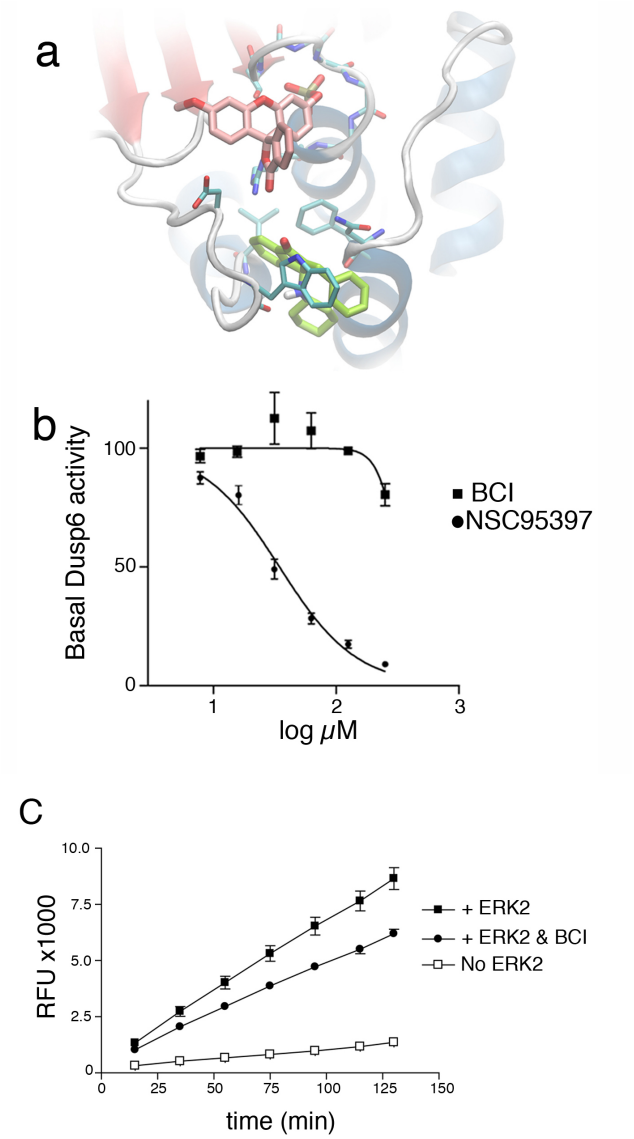

Supplementary Figure 5

BCI suppresses substrate-induced activation of Dusp6

(**a**) Docking simulations of OMFP (pink) and BCI (green) suggest that both can simultaneously bind Dusp6 at non-overlapping locations. (**b**) BCI did not suppress Dusp6 basal phosphatase activity toward OMFP. NSC95397, a broad-spectrum dual specificity phosphatase inhibitor, blocked basal Dusp6 activity toward OMFP. (**c**) A 10-fold excess of ERK2 (2.1 μg) stimulated (210 ng) Dusp6 dephosphorylation of OMFP by 6.5-fold and this induction was blocked by BCI. RFU, Relative Fluorescent Units were measured at excitation/emission wavelengths of 485/525nm.

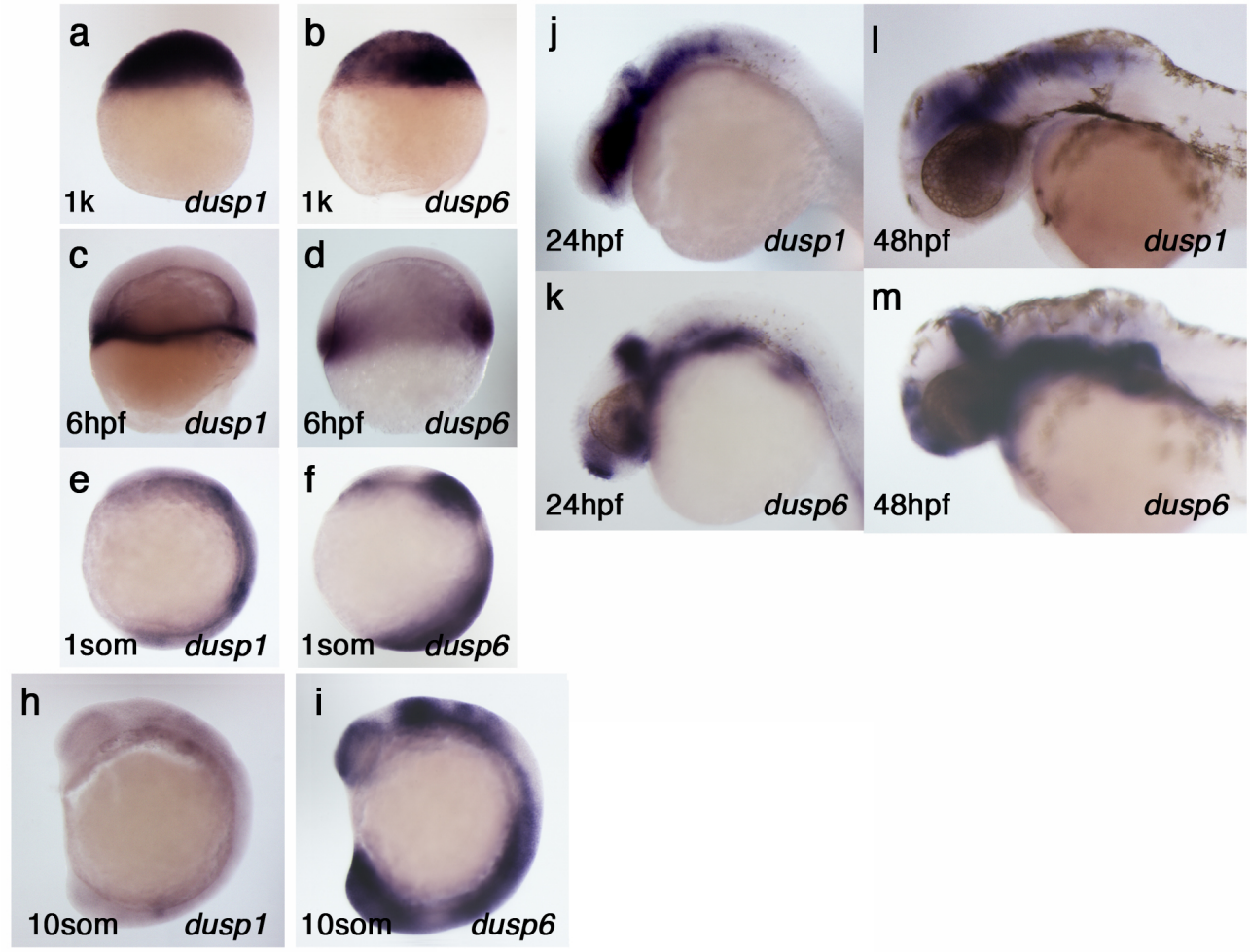

Supplementary Figure 6

Comparison of *dusp6* and *dusp1* expression in zebrafish.

(**a-m**) Lateral views of zebrafish embryos stained for *dusp1* or *dusp6* probe at the stages as indicated.

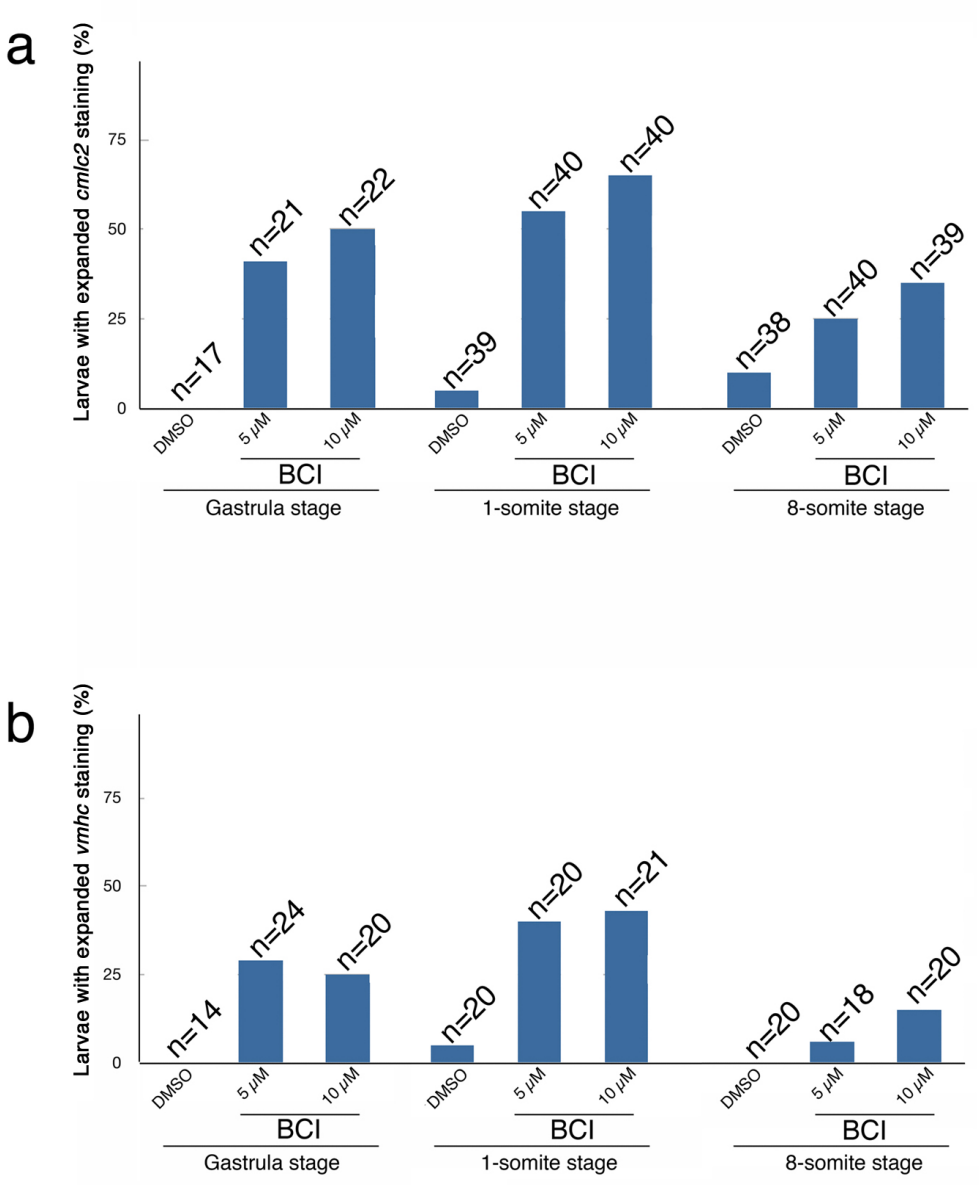

Supplementary Figure 7

BCI treatment from gastrula stage onwards resulted in enlarged hearts
(**a & b**) Graph showing BCI treatment resulted in cardiac expansion as measured by *cmlc2* and *vmhc* expression. Note that by the 8-somite stage, the ability of BCI to induce heart expansion was reduced.

Supplementary Methods

Docking Simulations

A two-step process was adopted for predicting the optimal binding poses of BCI and assessing the potential mechanism of inhibition. First, unbiased docking simulations were performed where the target protein (Dusp6) was assumed to be rigid either in the low-activity state or the high-activity state. These simulations permitted us to build two hypotheses, one of which was supported by more detailed flexible docking simulations. In the following the method and results from the two successive steps are described in more details.

1. Unbiased docking simulations

BCI was docked onto two different conformations of Dusp6 (MKP3): the low-activity form determined by X-ray crystallography (PDB ID: 1MKP)[1] and the high-activity form obtained by homology modeling using ORCHESTRAR (Tripos, Inc., St. Louis, MO). We used as templates the structures of Dusp9 (MKP4; PDB ID: 2HXP; 80% sequence identity), Dusp10 (MKP5; PDB ID: 1ZZW; 47% sequence identity), and Dusp5 (VH3; PDB ID: 2G6Z; 44% sequence identity) in the high-activity state[2-4]. For BCI, 400 docking poses (200 per enantiomer) were generated using AutoDock4 for each conformation[5,6]. Genetic algorithm population size was set to 250. Each docking pose was selected based on the energetic evaluation of up to 5×10^6 alternative conformations. The analysis of the resulting poses using an agglomerative clustering scheme revealed the clustering of a subset of binding poses in the vicinity of the active site in both conformations. In the low-activity state (**Fig. 5a**), the binding site was a crevice known to close upon catalytic activation of the enzyme. In the high-activity state (**Supplementary Fig. 3**) this crevice is not accessible. Instead, a relatively more hydrophobic patch in the neighborhood of the active site was predicted to serve as an alternative binding site for

the inhibitor[7]. Based on these observations two potential inhibition mechanisms were hypothesized:

(i) BCI binds the low-activity form of Dusp6 and restricts the mobility of the general acid loop so as to prevent ERK2 from inducing the conformational changes that lead to Dusp6 catalytic activation. This restricts ERK2 dephosphorylation to a basal catalytic rate.

(ii) BCI binds the ERK-actived Dusp6, and prevents ERK2 from optimally orienting itself, which leads to the inhibition of ERK2 dephosphorylation.

In either case, BCI was not expected to prevent Dusp6-ERK2 complex formation due to the large surface area of interaction distributed over two domains of Dusp6[8].

2. Flexible docking

Toward an assessment of the more likely inhibition mechanism among those hypothesized above, we further explored the binding properties of BCI by allowing the protein to undergo structural fluctuations in the neighborhood of the two above-defined states. Backbone flexibility was deduced from normal mode analysis and homology modeling calculations. Conformations accessible near the basal-activity state were sampled by using the anisotropic network model (ANM) in combination with all-atom energy minimization[9]. Third, fourth, and fifth ANM slow modes were found to set in motion the catalytic Asp262 close to the catalytic cavity (**Movie 1**) (see at ANM web server www.ccbb.pitt.edu/anm/ using the PDB ID 1MKP)[10]. The general acid loop was also observed to have a tendency to move towards the catalytic cavity in 10 ns long unbiased molecular dynamics simulations, in line with AMN calculations. NAMD software and the Charmm force field were used for energy minimization[11,12]. For each α-carbon, harmonic restraints with a force constant of 40 kcal/mole/Å^2 were defined to drive the

motions along the selected ANM modes at steps of size < 0.2 Å, similar to recently introduced ANM-steered simulations[13]. A total of twenty conformations were sampled along the selected modes by jointly optimizing backbone and side-chain conformations[14]. As for the high-activity state, multiple models generated with MODELLER were used as targets[15]. Asp262, Trp264, and Asn335 side chains were allowed to sample rotameric states from Penultimate library[14].

At least 1000 docking poses for the basal and activated state were generated using GOLD and cluster analysis was performed[15]. Docking poses were scored using GoldScore, which is a weighted sum of van der Waals energy and hydrogen bond energy that implicitly accounts for charged interactions[16]. The most populated and energetically favorable clusters were examined to identify the most favorable docking solution (**Fig. 5b**). The most favorable cluster of BCI docking poses was located in the low-activity conformation. The corresponding GoldScore averaged over all binding poses for this cluster was found to be 47.2 ± 2.1, in favor of the hypothesis (i).

Finally, as a further verification, docking simulations were performed to compare the binding properties of BCI against Dusp5, Dusp1 and Dusp6. BCI was docked onto to the crystal structure of Dusp5 (PDB ID: 2G6Z) and a model of Dusp1 based on Dusp6 structure using the same procedure as described above for Dusp6. Docking to the Dusp5 crystal structure yielded much lower docking scores (27.9 ± 1.4) due to lack of the crevice observed in Dusp6 (**Supplementary Fig. 4b**), explaining lack of activity against this constitutively active homolog. Docking of BCI to the Dusp1 model resulted in comparable interaction but lower Goldscores (37.4 ± 2.9) (**Supplementary Fig. 4a**).

Dusp6 movies

The Dusp6 movies were generated using energy minimization with harmonic constraints based on ANM modes, implemented following the procedure described in

our recent work[13]. **Movie 1**, which shows intrinsic flexibility of the general acid loop was generated using 3rd, 4th, and 5th slow modes. **Movie 2**, which shows the catalytic activation of Dusp6 was generated using 5% of the entire spectrum of modes in the low frequency regime.

Movie 1. Dusp6 intrinsic flexibility of the general acid loop was generated using 3rd, 4th, and 5th slow modes.

Movie 2. Catalytic activation of Dusp6 was generated using 5% of the entire spectrum of modes in the low frequency regime. The movie shows predicted confirmation shift of the general acid loop upon substrate binding.

Expression analyses of *dusp1* and *dusp6*

We compared the expression of *dusp1* and *dusp6* to determine if these genes are expressed in the same domains during development. At early stages, *dusp1* was ubiquitous while *dusp6* initiates within the prospective dorsal region of the embryo (**Supplementary Fig. 6a,b**)[17]. During gastrulation, both genes are expressed within the mesoderm and by somitogenesis stage *dusp1* was weak and diffuse, while *dusp6* was detected in the developing brain, the anterior lateral plate mesoderm (ALPM), somites and tailbud (**Supplementary Fig. 6c-i**). By 1dpf, both genes are expressed in the brain and continue to be expressed in this region at 2dpf (**Supplementary Fig. 6j-m**).

RT-PCR

Zebrafish embryos were treated at 24 hpf for 6 hours with BCI at 10 μM and 20 μM followed by total RNA extraction with Trizol (Invitrogen). cDNA synthesis with SuperScript II Reverse Transcriptase (Invitrogen) was performed as described by

manufacture's protocol and by Tsang et al.[17]. For PCR reaction, HotMaster Taq (Eppendorf) was used with the following primers:

Dusp6: For 5'-CGTTCAGAGGGGTTGTCCG-3'

Dusp6: Rev 5'-CTTCCCTGAACAGGAGACCC-3'

Spry4: For 5'-GCGGAGCAGCCCAAGATACT-3'

Spry4: Rev 5'-CAGGCAGGGCAAAACCAATGAG-3'

Sef: For 5'-CCAGTCAGGACGCGGGTTCAT-3'

Sef: Rev5'-GTTAAAGTGGCGCTGCGAGTGGAG-3'

Histone H4: For 5'-CACGAAACCCGCCATCCGTCG-3'

Histone H4: Rev 5'-GTACAGAGTGCGTCCCTGCCG-3'

Cycle conditions were: 94^{o}C 30 sec, 55^{o}C 45 sec, 72^{o}C 40 sec, for 25 cycles. PCR products were resolved on 3% agarose gels.

Whole mount *in situ* hybridization

In situ hybridization experiments were carried out as described previously[18]. The probes *eng3*, *krox20*, *sef*, *dusp6*, *gata4*, *nkx2.5*, *cmlc2*, *vmhc*, *scl*, *etsrp* and *hand2* were generated with a RNA labeling kit (Roche)[17,19-26]. The double fluorescent *in situ* hybridization protocol was kindly provided by Deborah Yelon and carried out as described by Schoenbeck et al.[27]. Fluorescent *in situ* hybridizations were visualized by confocal microscopy. Single optical sections and z-series of flat-mounted stained embryos were collected with a confocal laser scan head (SP5, Leica Microsystems, Inc.) mounted on an inverted compound microscope (DMI6000, Leica Microsystems, Inc.). Images were scanned and compiled with NIH ImageJ software (http://rsb.info.nih.gov/ij/).

***In vitro* ERK2 dephosphorylation assay.**

ERK2 dephosphorylation assays were performed as described previously with several modifications[7]. Briefly, recombinant His-tagged Dusp6 (1.5 ng) was expressed from a bacterial expression vector (a gift from Dr. Zhong-Yin Zhang, Indiana University, Indianapolis) and incubated for 20 minutes at 25°C in the presence of 100 μM BCI, 100 μM ICD or 1 mM sodium orthovanadate. Tyrosine and threonine phosphorylated ERK2 (New England Biolabs; 10 ng) was added and the reaction mixture (30 mM Tris-HCl, pH 7.0, 75 mM NaCl, 0.67 mM EDTA, 1 mM DTT and 0.033% bovine serum albumin) was incubated at 25°C for a further 60 min. ERK desphosphorylation was determined by Western blotting using 10% Tris-glycine gels and a monoclonal phospho-p44/42 MAPK antibody (Cell Signaling) at 1:1000 dilution. Total ERK was measured as a loading control using an anti-ERK antibody (Cell Signaling).

Dusp6, Cdc25B, PTP1B and VHR in vitro assays

Enzyme activities in the presence or absence of BCI were measured using the artificial substrate 3-*O*-methylfluorescein (OMFP) at concentrations equal to the K_m of each enzyme and at optimal pH for individual enzyme activity in a 96-well microtiter plate assay based on previously described[28,29]. Briefly, the standard assay conditions contained 0.02 mg/ml OMFP in assay buffer (30 mM Tris-HCl (pH8.0), 75 mM NaCl, 1 mM EDTA, 0.33% BSA and 1 mM DTT). OMFP was added at its apparent Km for each phosphatase[30]. The final reaction volume was 15 μl. Fluorescence emission was measured after a sixty-minute incubation period at ambient temperature using a multiwell plate reader (SpectraMax m5, Applied Biosystems; excitation 485nm, emission 525nm). Sodium orthovanadate (100 μM) was used as a positive control for full phosphatase inhibition or in the Dusp6 assay, with 2,3-bis(2-hydroxyethylthio)naphthalene-1,4-dione) (NSC95397, **6**), a broad spectrum dual

specificity phosphatase inhibitor[31]. IC_{50} values were determined from three experiments using 10 concentrations of BCI ranging from 300 μM to 15.2 nM and GraphPad Prism 5.0 software.

Dusp6 activation assay

To assay substrate-induced Dusp6 activation, Dusp6 (210 ng) was added to a solution of BCI (100 μM) containing 2.1 μg or 210 ng of recombinant ERK2 (Cell signaling) to generate 1:1 and 1:10 enzyme to substrate ratios. OMFP was immediately added and fluorescence (ex485/em525nm) was read every 10 min for 130 min. Fold activation was calculated at 60mins in each experiment. Percent inhibition of the activatable portion of Dusp6 activity was calculated as $1-((RFU_{(BCI,\ +Erk)} - RFU_{(-Erk)}) / (RFU_{(+Erk)} - RFU_{(-Erk)})) \times 100$.

Synthesis of BCI and related analogs.

We independently synthesized BCI by aldol condensation of 2,3-dihydro-1*H*-inden-1-one with benzaldehyde, bromination and S_{N2} addition of cyclohexylamine for subsequent studies. (*E*)-2-Benzylidene-2,3-dihydro-1*H*-inden-1-one (BI) and 3-(cyclohexylamino)-2,3-dihydro-1*H*-inden-1-one (ICD) were prepared by bromination of 2,3-dihydro-1*H*-inden-1-one and displacement of bromide with cyclohexylamine. All reactions were conducted in oven-dried glassware under a dry atmosphere. Starting materials, reagents and anhydrous solvents were purchased from commercial suppliers (Sigma-Aldrich and Fisher). Reactions were monitored by TLC on EM Science pre-coated silica gel 60 F_{254} plates, 250 μm layer thickness. Flash chromatography was performed over silica gel 60, 230-400 mesh. Low resolution mass spectra (MS) were obtained in electron ionization (EI) mode on a Hewlett Packard 5971 mass selective detector coupled to a Hewlett Packard 5890 Series II gas chromatograph equipped with a 30 m 5% phenyl methylsilicone capillary column from Supelco. High resolution mass spectra (HRMS) were obtained with an Applied Biosystems 4700 MALDI-TOF instrument using α-cyano-4-hydroxycinnamic acid as the matrix. Melting points were determined on a Fisher-Johns open stage apparatus and are uncorrected. ^{1}H and ^{13}C NMR spectra were recorded on a Varian Mercury spectrometer at 400 and 100 MHz, respectively, or a Bruker Avance spectrometer at 600 and 150 MHz, respectively. NMR chemical shifts were referenced to the residual $CHCl_3$ signal (7.26 ppm downfield from Me_4Si) and ^{13}C NMR chemical shifts to the solvent $CDCl_3$ signal (77.00 ppm downfield from Me_4Si), respectively.

(*E*)-2-Benzylidene-2,3-dihydro-*1H*-inden-1-one

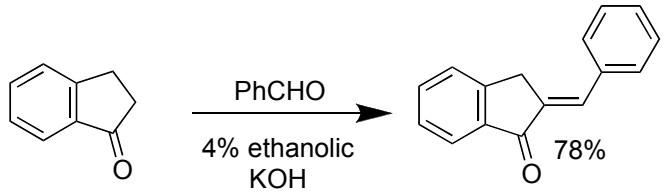

(*E*)-2-Benzylidene-2,3-dihydro-*1H*-inden-1-one (BI) was synthesized as described by Hassner and Cromwell[32]. An ice bath-cooled mixture of 2,3-dihydro-1*H*-indan-1-one (2.0 g, 15.1 mmol) and benzaldehyde (1.6 g, 15.1 mmol) was treated dropwise with 4% ethanolic KOH (*w/v*) with stirring until precipitation ceased. After an additional 1 h of stirring at room temperature, the precipitate was collected by filtration, washed with cold H_2O, then recrystallized from MeOH-H_2O to give the title compound as straw-colored crystals (2.6 g, 78% yield): M.p. 109-110 ^oC (lit.[1] 109-110 ^oC); ^1H NMR (400 MHz, $CDCl_3$): δ 4.07 (s, 2H), 7.34–7.78 (m, 9H), 7.94 (d, 1H, *J*=7.6 Hz); ^{13}C NMR (100 MHz, $CDCl_3$): δ 33.3, 125.1, 128.0, 129.1, 130.5, 131.6, 132.6, 134.8, 136.4, 137.3, 139.6, 151.4, 194.3; MS (EI) *m/z* (relative intensity): 220 ($M^{+\bullet}$, 55), 219 (M-1, 100). HRMS (MALDI-TOF) calc'd for *m/z* 221.0966 $[M+H]^+$, found 221.0970. CAS Registry No: [17434-21-8].

(*Z*)-2-Benzylidene-3-bromo-2,3-dihydro-1*H*-inden-1-one

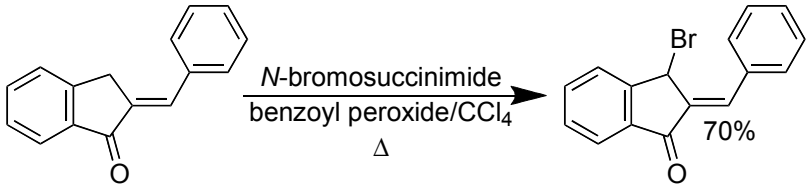

(*Z*)-2-Benzylidene-3-bromo-2,3-dihydro-1*H*-inden-1-one (ICD) was generated as described by Pearson et. al.[33]. Briefly, (*E*)-2-Benzylidene-2,3-dihydro-*1H*-inden-1-one (1.0 g, 4.5 mmol), *N*-bromosuccinimide (0.8 g, 4.5 mmol) and benzoyl peroxide (61 mg, 0.25 mmol) were dissolved in 15 mL of CCl_4. The mixture stirred and heated to reflux for 1 h under a N_2 atmosphere. The mixture was cooled to r.t. and stirred an additional 1 h. After filtration and concentration from solvent under vacuum, the resulting orange solid was recrystallized three times from CCl_4 to give the title compound as a straw-colored solid (0.94 g, 70% yield): M.p. 118-119 ^{o}C (lit.[2] 119-120 ^{o}C); ^{1}H NMR (400 MHz, $CDCl_3$): δ 6.33 (s, 1H, C3-H), 7.19-7.85 (m, 10H, 9 aromatic, 1 vinyl); ^{13}C NMR (100 MHz, $CDCl_3$): δ 39.9, 127.4, 127.8, 128.4, 128.6, 128.7, 129.4, 134.1, 134.9, 135.6, 139.6, 141.9, 149.4, 192.8; MS (EI) *m/z* (relative intensity): 296 ($[^{77}Br]M^{+\bullet}$, 14); HRMS (MALDI-TOF) calc'd for *m/z* 297.0102 $[[^{77}Br]M+H]^{+}$, found 297.0096. CAS Registry No: [5387-50-8].

(*E*)-2-Benzylidene-3-(cyclohexylamino)-2,3-dihydro-1*H*-1-one

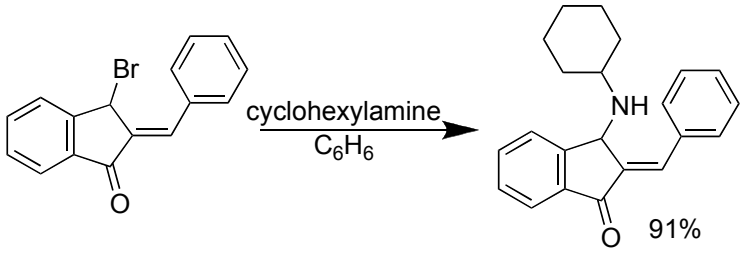

(*E*)-2-Benzylidene-3-(cyclohexylamino)-2,3-dihydro-1*H*-1-one (BCI) was synthesized as described by Maury et al.[34]. (*Z*)-2-Benzylidene-3-bromo-2,3-dihydro-1*H*-inden-1-one (212 mg, mmol) and cyclohexylamine (161 mg, mmol) were dissolved in 15 mL of dry benzene and stirred at r.t. under N_2 for 1 h. Cyclohexylamine•HBr was removed by filtration and the filtrate was concentrated under vacuum to give a yellow oil. This was purified by flash chromatography (SiO_2, 50:3 hexanes-EtOAc) to give a pale yellow solid M.p. 94-95 ^oC (lit.[3] 94-96 ^oC); ^1H NMR (600 MHz, $CDCl_3$): δ 0.906-1.710 (m, 11H), 2.360-2.410 (m, 1H, NH), 5.384 (s, 1H, C3-H), 7.345-7.521 (m, 4H), 7.639-7.682 (m, 2H), 7.741 (s, vinyl H) 7.885-7.941, m 3H); ^{13}C NMR (150 MHz, $CDCl_3$): δ 24.79, 24.92, 25.83, 33.86, 34.84, 52.53, 55.34, 124.11, 126.21, 128.62, 128.66, 129.70, 131.40, 134.59, 134.85, 135.90, 137.45, 138.51, 152.97, 193.65; MS (EI) *m/z* (relative intensity): 317 ($M^{+\bullet}$, 9); HRMS (MALDI-TOF) calc'd for *m/z* 318.1858 $[M+H]^+$, found 318.1869. CAS Registry No: [15982-84-0].

3-Bromo-2,3-dihydro-1*H*-inden-1-one

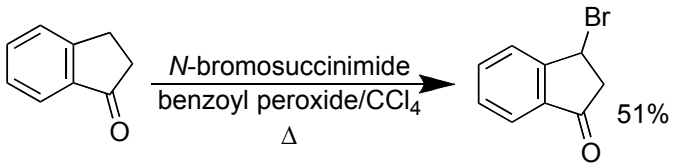

3-Bromo-2,3-dihydro-1*H*-inden-1-one was generated as described by Treibs and Schroth [35]. 2,3-Dihydro-1*H*-indan-1-one (528 mg, 4 mmol), *N*-bromosuccinimide (684 mg, 4 mmol) and benzoyl peroxide (30 mg, 0.12 mmol) were dissolved in CCl_4 (10 mL) and heated to reflux for 1h under an N_2 atmosphere. After cooling, succinimide was removed by filtration and the filtrate concentrated under high vacuum to yield the title compound as a straw-colored oil of > 99% purity as seen by GC-MS and NMR that was used without further purification (428 mg, 51% yield). ^{1}H NMR (600 MHz, $CDCl_3$): δ 3.064 (dd, 1H, *J*=19.7, *J*=2.3 Hz, CH_2), 3.370 (dd, 1H, *J*=19.7Hz, *J*=7.2Hz, CH_2) 5.609 (dd, 1H, *J*=7.2Hz, *J*=2.6Hz, C3-H), 7.468-7.520 (m, 1H), 7.702-7.775 (m, 3H); ^{13}C NMR (150 MHz, $CDCl_3$): δ 40.28, 50.30, 127.29, 128.81, 128.86, 133.72, 138.00, 204.55; MS (EI) *m/z* (relative intensity): 208 ([^{77}Br]$M^{+\bullet}$, 22). CAS Registry No: [40774-41-2].

3-(Cyclohexylamino)-2,3-dihydro-1*H*-inden-1-one

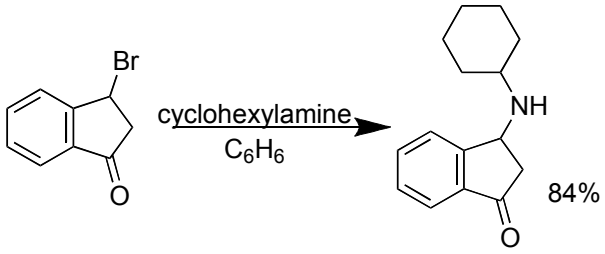

3-Bromo-2,3-dihydro-1*H*-inden-1-one (100 mg, 475 μmol) and cyclohexylamine (94 mg, 951 μmol) were dissolved in 2 mL of dry benzene and stirred under N_2 until precipitation ceased (~15 min). The cyclohexylamine•HBr was removed by filtration. The filtrate was applied to a flash SiO_2 column that was developed with 8:1 hexanes-EtOAc to give the title compound as a clear oil (91 mg, 84% yield). ^{1}H NMR (600 MHz, $CDCl_3$): δ 1.059-1.205 (m, 4H), 1.207-1.344 (m, 2H), 1.591-1.646 (m, 1H), 1.696-1.825 (m, 3H), 1.953-2.045 (m, 1H), 2.446 (dd, *J*=18.63Hz, *J*=3.09Hz, 1H), 2.600-2.675 (m, 1H), 2.953 (dd, *J*=6.72Hz, *J*=18.60Hz, 1H), 4.517 (dd, *J*=6.58Hz, *J*=3.00Hz, 1H), 7.384 (dd, *J*=7.34Hz, *J*=0.89Hz, 1H), 7.594 (dd, *J*=7.14Hz, *J*=0.90Hz, 1H), 7.632 (d, *J*=7.74Hz, 1H), 7.689 (d, *J*=7.68Hz, 1H); ^{13}C NMR (150 MHz, $CDCl_3$): δ 24.73, 24.92, 25.94, 33.12, 34.47, 46.01, 53.07, 55.23, 123.14, 125.83, 128.41, 134.73, 136.52, 156.61, 204.77; MS (EI) *m/z* (relative intensity) 229 ($M^{+\bullet}$, 40), 186 (90), 131 (100); HRMS (MALDI-TOF) calc'd for *m/z* 230.1545 $[M+H]^+$, found 230.1550.

References:

1. Stewart, A.E., Dowd, S., Keyse, S.M. & McDonald, N.Q. Crystal structure of the MAPK phosphatase Pyst1 catalytic domain and implications for regulated activation. *Nat Struct Biol* 6, 174-81 (1999).
2. Almo, S.C. et al. Structural genomics of protein phosphatases. *J Struct Funct Genomics* 8, 121-40 (2007).
3. Jeong, D.G. et al. Crystal structure of the catalytic domain of human DUSP5, a dual specificity MAP kinase protein phosphatase. *Proteins* 66, 253-8 (2007).
4. Jeong, D.G. et al. Crystal structure of the catalytic domain of human MAP kinase phosphatase 5: structural insight into constitutively active phosphatase. *J Mol Biol* 360, 946-55 (2006).
5. Huey, R., Morris, G.M., Olson, A.J. & Goodsell, D.S. A semiempirical free energy force field with charge-based desolvation. *Journal of Computational Chemistry* 28, 1145-1152 (2007).
6. Morris, G.M. et al. Automated docking using a lamarckian genetic algorithm and an empirical binding free energy functions. *Journal of Computational Chemistry* 19, 1639-1662 (1998).
7. Lazo, J.S. et al. Structurally unique inhibitors of human mitogen-activated protein kinase phosphatase-1 identified in a pyrrole carboxamide library. *J Pharmacol Exp Ther* 322, 940-7 (2007).
8. Zhou, B. et al. Mapping ERK2-MKP3 binding interfaces by hydrogen/deuterium exchange mass spectrometry. *J Biol Chem* 281, 38834-44 (2006).
9. Atilgan, A.R. et al. Anisotropy of fluctuation dynamics of proteins with an elastic network model. *Biophys J* 80, 505-15 (2001).
10. Eyal, E., Yang, L.W. & Bahar, I. Anisotropic network model: systematic evaluation and a new web interface. *Bioinformatics* 22, 2619-27 (2006).
11. MacKerell Jr., A.D. et al. All-Atom Empirical Potential for Molecular Modeling and Dynamics Studies of Proteins. *J. Phys. Chem.* 102, 3586-3616 (1998).
12. Phillips, J.C. et al. Scalable molecular dynamics with NAMD. *J Comput Chem* 26, 1781-802 (2005).
13. Isin, B., Schulten, K., Tajkhorshid, E. & Bahar, I. Mechanism of Signal Propagation upon Retinal Isomerization: Insights from Molecular Dynamics Simulations of Rhodopsin Restrained by Normal Modes. *Biophys J* 95, 789-803 (2008).
14. Lovell, S.C., Word, J.M., Richardson, J.S. & Richardson, D.C. The penultimate rotamer library. *Proteins* 40, 389-408 (2000).
15. Jones, G., Willett, P., Glen, R.C., Leach, A.R. & Taylor, R. Development and validation of a genetic algorithm for flexible docking. *J Mol Biol* 267, 727-48 (1997).
16. Jones, G., Willett, P. & Glen, R.C. Molecular recognition of receptor sites using a genetic algorithm with a description of desolvation. *J Mol Biol* 245, 45-53 (1995).
17. Tsang, M. et al. A role for MKP3 in axial patterning of the zebrafish embryo. *Development* 131, 2769-79 (2004).

18. Kudoh, T. et al. A gene expression screen in zebrafish embryogenesis. *Genome Res* 11, 1979-87 (2001).
19. Chen, J.N. & Fishman, M.C. Zebrafish tinman homolog demarcates the heart field and initiates myocardial differentiation. *Development* 122, 3809-16 (1996).
20. Ekker, M., Wegner, J., Akimenko, M.A. & Westerfield, M. Coordinate embryonic expression of three zebrafish engrailed genes. *Development* 116, 1001-10 (1992).
21. Liao, E.C. et al. SCL/Tal-1 transcription factor acts downstream of cloche to specify hematopoietic and vascular progenitors in zebrafish. *Genes Dev* 12, 621-6 (1998).
22. Oxtoby, E. & Jowett, T. Cloning of the zebrafish krox-20 gene (krx-20) and its expression during hindbrain development. *Nucleic Acids Res* 21, 1087-95 (1993).
23. Pham, V.N. et al. Combinatorial function of ETS transcription factors in the developing vasculature. *Dev Biol* 303, 772-83 (2007).
24. Tsang, M., Friesel, R., Kudoh, T. & Dawid, I.B. Identification of Sef, a novel modulator of FGF signalling. *Nat Cell Biol* 4, 165-9 (2002).
25. Yelon, D., Horne, S.A. & Stainier, D.Y. Restricted expression of cardiac myosin genes reveals regulated aspects of heart tube assembly in zebrafish. *Dev Biol* 214, 23-37 (1999).
26. Yelon, D. et al. The bHLH transcription factor hand2 plays parallel roles in zebrafish heart and pectoral fin development. *Development* 127, 2573-82 (2000).
27. Schoenebeck, J.J., Keegan, B.R. & Yelon, D. Vessel and blood specification override cardiac potential in anterior mesoderm. *Dev Cell* 13, 254-67 (2007).
28. Lazo, J.S. et al. Discovery and biological evaluation of a new family of potent inhibitors of the dual specificity protein phosphatase Cdc25. *J Med Chem* 44, 4042-9 (2001).
29. Lazo, J.S. et al. Novel benzofuran inhibitors of human mitogen-activated protein kinase phosphatase-1. *Bioorg Med Chem* 14, 5643-50 (2006).
30. Vogt, A. et al. The benzo[c]phenanthridine alkaloid, sanguinarine, is a selective, cell-active inhibitor of mitogen-activated protein kinase phosphatase-1. *J Biol Chem* 280, 19078-86 (2005).
31. Vogt, A. et al. A cell-active inhibitor of mitogen-activated protein kinase phosphatases restores paclitaxel-induced apoptosis in dexamethasone-protected cancer cells. *Mol Cancer Ther* 7, 330-40 (2008).
32. Hassner, A. & Cromwell, N. The Chemistry of derivatives of 2-benzaltetrahydro-naphthalenone. II. Absorption spectra and stereostructure. . *J Am Soc Chem* 80, 893-900 (1958).
33. Pearson, B., Ayer, R. & Cromwell, N. Elimination Reactions of a-Halogenated Ketons. IX. A Comparison of the Reactions of 2-Bromo-2-(a-bromobenzyl)-1-indanone with those of 2-Bromo-2-(a-bromobenzyl_-3-,3-dimethyle-1-indanone. *J Org Chem* 27, 3038-3044 (1962).
34. Maury, G., Wu, E. & Cromwell, N. Mobile Keto Allyl Systens. VI. Reaction of 3-Bromo-2-benzal-1-indanone with Amines. . *J Org Chem* 33, 1900-1907 (1968).
35. Treibs, W. & Schroth, W. 2-Indanone. Pseudoaromatic compounds from 2-indanones. *Justus Liebigs Ann Chem* 639, 204-213 (1961).